JOURNAL OF ADHESION SCIENCE AND TECHNOLOGY
2025, VOL. 39, NO. 5, 801–816
https://doi.org/10.1080/01694243.2024.2427785

Effects of current density on the corrosion resistance of micro-arc oxidation coatings on Ti6Al4V welded joints

Yinghe Ma[a,b,c], Zhen Yu[a,b], Yonghui Hu[a,b], Jianguo Yang[a,b] and Paul K. Chu[c]

[a]Institute of Process Equipment and Control Engineering, College of Mechanical Engineering, Zhejiang University of Technology, Hangzhou, China; [b]Engineering Research Center of Process Equipment and Remanufacturing, Ministry of Education, Zhejiang University of Technology, Hangzhou, China; [c]Department of Physics, Department of Materials Science and Engineering, and Department of Biomedical Engineering, City University of Hong Kong, Kowloon, Hong Kong, China

ABSTRACT

The effects of different current densities in micro-arc oxidation (MAO) on the microstructure and corrosion resistance of electron beam welded Ti6Al4V alloy joints are investigated by scanning electron microscopy (SEM), energy-dispersive X-ray spectroscopy (EDS), X-ray diffraction (XRD). The electrochemical corrosion behavior is studied in a 3.5% NaCl solution by polarization and electrochemical impedance spectroscopy (EIS). The thickness of the BM-MAO coating (base metal region) increases gradually with current densities and reaches a maximum at 16 A/dm^2. In comparison, the thickness of the WZ-MAO coating (welded zone) increases initially and reaches a maximum at 12 A/dm^2 before decreasing gradually. When the current density is 10–14 A/dm^2, the WZ-MAO coating is thicker than the BM-MAO coating. However, the thickness of the WZ-MAO coating is smaller at 16 A/dm^2. The BM-MAO and WZ-MAO coatings show decreased porosity with increasing current densities, and the porosity of the latter is lower. Dynamic potential polarization tests reveal a significant reduction in the self-corrosion current density at the BM area and welded joint (WJ), by an order and two orders of magnitude, respectively, after the application of MAO coatings with different current densities. The BM-MAO and WJ-MAO coatings deposited at a current density of 12 A/dm^2 exhibit optimal corrosion resistance. The corrosion resistance of BM-MAO coating is better than that of WJ-MAO at different current densities according to the equivalent resistance and dielectric behavior.

ARTICLE HISTORY
Received 18 September 2024
Revised 24 October 2024
Accepted 5 November 2024

KEYWORDS
Ti6Al4V; electron beam welded joints; micro-arc oxidation; current densities; corrosion resistance

1. Introduction

Titanium and its alloys are widely used in aerospace, marine engineering, and biomedical fields due to their excellent properties such as low density, high specific

CONTACT Jianguo Yang yangjg@zjut.edu.cn Institute of Process Equipment and Control Engineering, Zhejiang University of Technology, Hangzhou, China; Paul K. Chu paul.chu@cityu.edu.hk Department of Physics, Department of Materials Science and Engineering, and Department of Biomedical Engineering, City University of Hong Kong, Kowloon, Hong Kong, China.

strength, corrosion resistance, heat resistance, wide operating temperature range [1–3], high damping and superelasticity [4,5]. With the development of marine equipment and high-performance ships, the application of titanium alloys to the field of marine engineering has shown a trend of rapid growth and has become necessary material for the manufacture of high-performance structural components. They are used in various aspects of marine engineering, such as the exploration and development of marine resources, seawater desalination, pressure-resistant shells, engine parts, and so on. In marine equipment manufacturing, welding is an indispensable process. The proper welding method can improve the efficiency and quality of manufacturing [6,7]. However, titanium and its alloys are prone to corrosion in seawater environments due to changes in microstructure, reduced mechanical properties, and corrosion resistance of the joints after welding [8,9]. Therefore, it is necessary to protect the surface of titanium alloy joints. The micro-arc oxidation (MAO) technology generates a ceramic layer on the surface of titanium and its alloys to improve the wear resistance, corrosion resistance, and other properties and prolong the service life of the components [10–15]. Shokouhfar et al. investigated the effect of nanoparticle incorporation on the corrosion resistance of micro-arc oxidation (MAO) coatings on titanium alloys through the addition of various nanoparticles into the electrolyte. Their results demonstrated that the inclusion of nanoparticles effectively filled the micropores in the oxide film, reducing surface roughness and porosity, which in turn significantly improved the corrosion resistance of the MAO coating [16]. Sobolev et al. studied the influence of pulse frequencies ranging from 200 to 1000 Hz on the surface morphology and corrosion resistance of Ti6Al4V ceramic coatings. Their findings revealed that at a higher pulse frequency of 1000 Hz, the ceramic coating exhibited increased density and lower porosity. Compared to untreated titanium alloy, the ceramic coating produced at 1000 Hz showed significantly enhanced corrosion resistance [17]. Li et al. provided a comprehensive review of existing research on the micro-arc oxidation (MAO) of titanium alloys, examining key aspects such as the MAO mechanism, MAO electrolyte, process parameters—including current, voltage, pulse frequency, and oxidation time—as well as pre-treatment of titanium alloy substrates. The study emphasized that the MAO process plays a critical role in determining the properties of the oxide film formed on titanium alloy surfaces, which directly impacts the corrosion resistance of the coatings. However, while existing research primarily focuses on variations in current modes, voltage levels, pulse frequencies, and oxidation times, limited attention has been given to the effects of current density during MAO, especially regarding titanium alloy welded joints. Therefore, further investigation into the preparation of MAO coatings on titanium alloy welded joints and the evaluation of their corrosion resistance is essential for advancing the use of titanium alloy components in marine engineering applications [18–21]. Preliminary research has been reported in ref. [22], but further research is still needed.

The primary factors influencing the quality of MAO coatings are the electrolyte and electrical parameters [23,24]. In particular, the current density plays a pivotal role in determining the thickness, composition, and morphology of MAO coatings [25,26]. Herein, the effects of different MAO current densities (10, 12, 14, and 16 A/dm^2) in the Na_2SiO_3–Na_3PO_4 composite electrolyte on the base metal (BM) and

Table 1. Micro-arc oxidation electrolyte formulation.

Component	Na_2SiO_3	Na_3PO_4	NaOH
Concentration (g/L)	15	10	1

Table 2. Micro-arc oxidation process parameters.

Current density(A/dm^2)	Pulse frequency (Hz)	Duty cycle (%)	Oxidation time (min)
10	100	20	20
12	100	20	20
14	100	20	20
16	100	20	20

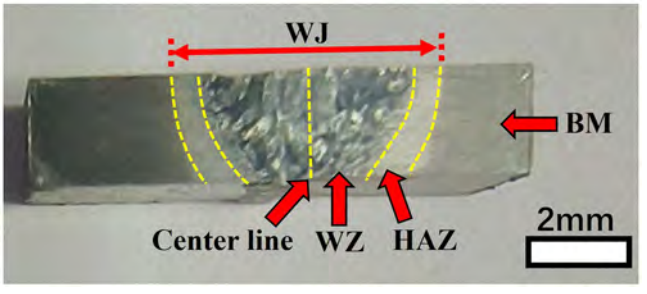

Figure 1. Macroscopic morphology of titanium alloy electron beam welded joints.

welding zone (WZ) coatings of Ti6Al4V electron beam welded joints (WJ) are investigated, especially the microstructure and corrosion resistance.

2. Materials and methods

2.1. Preparation of MAO coatings

The Ti6Al4V titanium alloy belongs to the category of (α + β) duplex titanium alloys [27]. The Ti6Al4V titanium alloy plates measuring 50 × 50 × 2 mm were polished with SiC sandpaper (ranging from 400# to 1200#), ultrasonically cleaned in acetone and alcohol, and air dried. The welding process adopted a high voltage of 65 kV, an electron beam current of 10 mA, a focusing current of 264 mA, and a speed of 300 mm/min. The electrolyte was a Na_2SiO_3-Na_3PO_4 and the composition is shown in Table 1.

MAO was conducted by the constant current mode as shown in Table 2. Perform micro arc oxidation treatment on different areas of the electron beam welded sample, as shown in Figure 1, which are divided into the base metal area (BM) and the welding area (WZ) of the welded joint (WJ).

2.2. Microstructure characterization

The surface and cross-sectional morphologies of the Ti6Al4V electron beam welded joints, both before and after the application of MAO coatings, were examined by scanning electron microscopy (SEM, Gemini 500) equipped with energy-dispersive

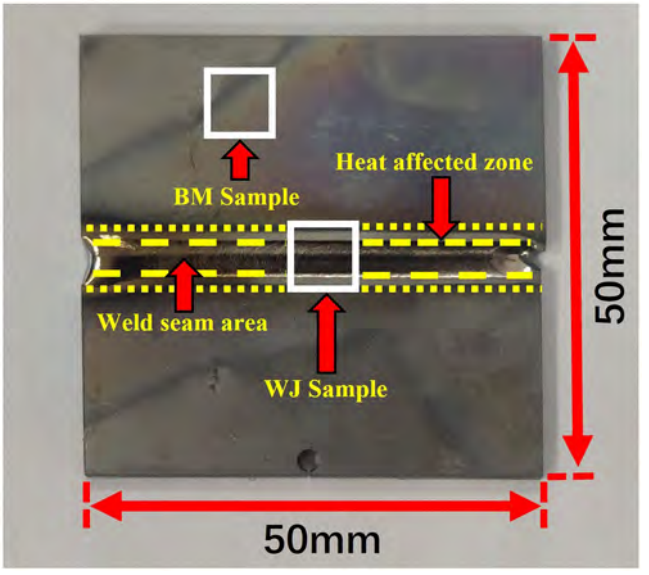

Figure 2. Sampling locations for electrochemical experiments in the base metal area (BM) and welded joint (WJ).

X-ray spectroscopy (EDS, Bruker D8 Advance). The phase composition of the Ti6Al4V electron beam welded joints and MAO coatings prepared with different current densities were analyzed by X-ray diffraction (XRD, X'PERT PRO).

2.3. Electrochemical tests

Electrochemical characterization was conducted using a CorrTest CS350H electrochemical workstation and the traditional three-electrode configuration. In this setup, the sample with an exposed area of 1 cm^2 was the working electrode. A platinum electrode functioned as the counter electrode, creating a circuit with the working electrode, while a saturated calomel electrode was the reference electrode. The selected areas for the samples of BM and WJ samples are shown in Figure 2. The experiments were performed at room temperature in a 3.5 wt.% NaCl solution. The potentiodynamic polarization test was conducted at a scanning rate of 10 $mV \cdot s^{-1}$ and a scanning range of −1 ~ 2 V (vs. OCP). Electrochemical impedance spectroscopy (EIS) was conducted in a frequency range of 100 kHz to at 10^{-1} Hz and 10 mV around the OCP. The required time to reach a steady state was 2 h. Each style undergoes three repeated tests to ensure the accuracy of the test data.

3. Results

3.1. Microstructure of titanium alloy electron beam welded joints

Figure 3 shows the microstructure of different regions in the electron beam welded joint of Ti6Al4V titanium alloy. Figure 3a indicates that the primary microstructure of the base material (BM) region is composed of the primary alpha phase (dark

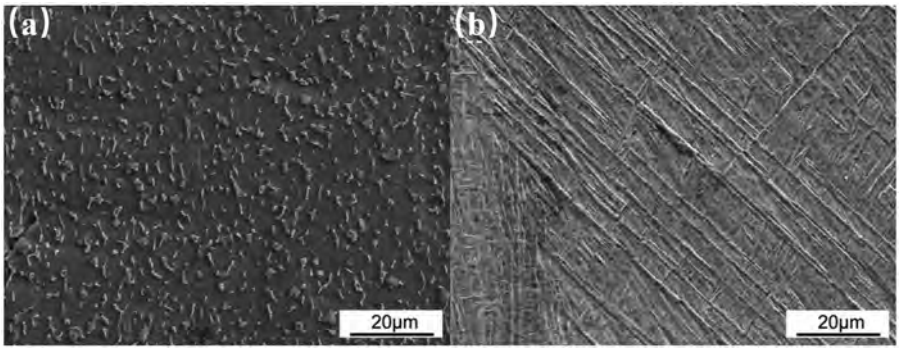

Figure 3. SEM images in (a) base material (BM); (b) welded zone (WZ).

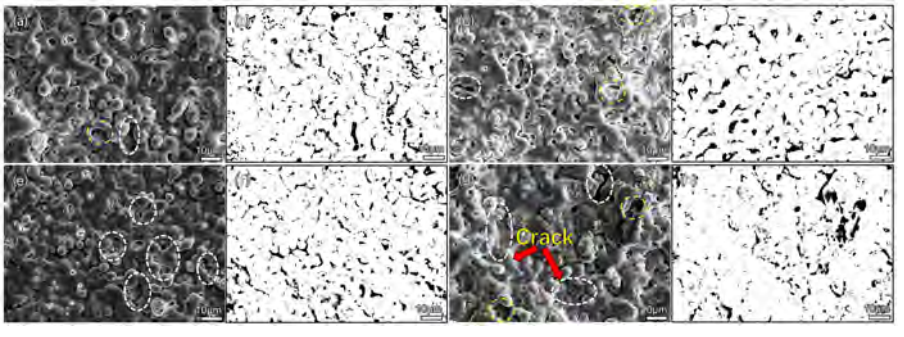

Figure 4. Surface morphology and pore distribution of BM-MAO coatings for different current densities: (a) 10 a/dm^2; (b) 12 a/dm^2; (c) 14 a/dm^2; (d) 16 a/dm^2.

color) and the intergranular beta phase (bright color). Figure 3b shows that the needle shaped α′ martensite is the main microstructure of the WZ in Ti6Al4V after electron beam welding. α′ martensite with the same orientation nucleates and precipitates at the β grain boundary, and is distributed in a feather shape [28]. There is also some needle shaped α′ martensite with irregular distribution and vertical growth [29].

3.2. Effects of current density on the surface morphology of MAO coatings

The surface morphology and pore distribution in the MAO coatings on the base metal (BM-MAO) and welded zone (WZ-MAO) using different current densities are depicted in Figure 4 and Figure 5, respectively. The surface morphologies of MAO-BM and MAO-WZ coatings are similar, with the oxide film surface being covered by molten materials and showing a heterogeneous distribution of micropores resembling volcanos. These micropores predominantly manifest in two shapes: elongated and elliptical [30]. A larger current density increases the amount of molten materials on the coating surface, changes the surface roughness, reduces the number of micropores, and displays a trend in which the overall micropore size initially increases and then decreases.

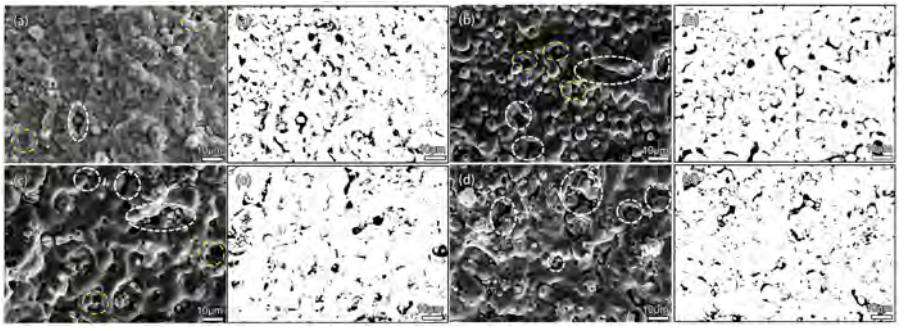

Figure 5. Surface morphology and pore distribution of WZ-MAO coatings for different current densities: (a) 10 a/dm^2; (b) 12 a/dm^2; (c) 14 a/dm^2; (d) 16 a/dm^2.

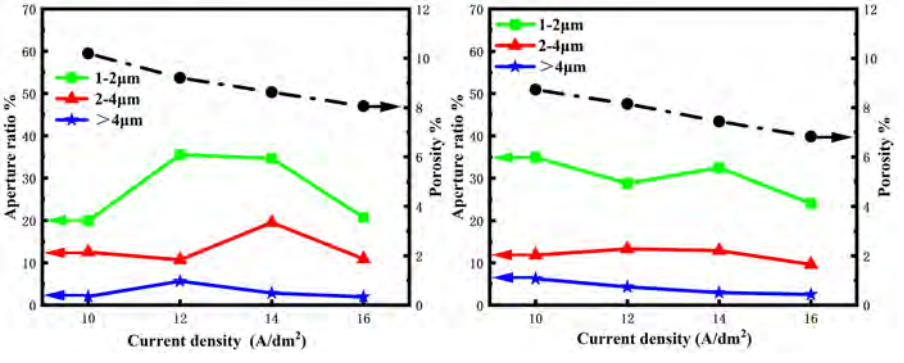

Figure 6. Aperture ratio and porosity of (a) BM-MAO coating and (b) WZ-MAO coating for different current densities.

The surface morphology can be attributed to two primary factors. First, upon reaching the breakdown voltage, anions in the electrolyte migrate toward the substrate and enter the discharge channel driven by the electric field. At the same time, under high pressure and temperature conditions, the weaker points on the surface are preferentially breached, thus initiating a series of chemical reactions in the electrolyte to form molten oxidation products. These products are then expelled from the discharge channel due to the high pressure, cooled by the electrolyte, and subsequently deposited on the substrate surface to create a crater-like morphology. Furthermore, the gas discharge arising from these reactions further contributes to crater formation. Figures 4 and 5 also reveal the presence of numerous microcracks in the MAO coatings stemming from high thermal stress during rapid cooling upon contact with the electrolyte [31–34].

Figure 6, respectively, illustrates the porosity and pore size of the BM-MAO and WZ-MAO coatings. Figure 6 indicates that micropores with sizes of 1–2 μm are the majority in the BM-MAO and WZ-MAO coatings. Therefore, pores smaller than 1 micrometer are not considered. This predominance of smaller pores during the initial stages of micro-arc oxidation is because the lower energy generates primarily small holes. As the current density and energy increase, the reactions intensify to produce more small holes. These pores, mainly volcanic in shape (indicated by

yellow circles), evolve as multiple smaller pores fuse to create larger apertures predominantly elongated in shape (indicated by white circles), thereby increasing the proportion of pores larger than 2 μm. As the current density increases (such as 16 A/dm^2), more melt forms, leading to a self-sealing of pores and closure of large-aperture micropores. This results in a gradual decrease in the percentage of pores and an overall larger surface roughness of the MAO coating.

Figure 6 shows that the coatings fabricated on both BM and WZ regions demonstrate a decrease in porosity with increasing current densities. This reduction in porosity arises from that the molten materials cover some of the micropores and enhance self-sealing at higher current densities. As the current density goes up, the melted area produces more self-sealing holes. The cycle of melting and cooling decreases the micropore numbers. In addition, at different current densities, the porosity of WZ-MAO coatings is slightly lower than that of BM-MAO coatings. This is largely because of the longer and larger frequency of self-sealing. The phenomenon is primarily due to the microstructural characteristics of the WZ region, which predominantly consists of coarse metastable needle-like α′ martensite before MAO [35, 36]. This form of martensite exhibits a higher susceptibility to micro-arc oxidation reactions. In comparison with other regions, the welded zone experiences micro-arc oxidation reactions that not only last longer and occur more frequently, but also possess greater energy. This combination of factors contributes to less porosity during this process.

3.3. Effects of current densities on the thickness of MAO coatings

Figures 7 and 8 illustrate the cross-sectional morphologies of the BM and WZ regions subjected to micro-arc oxidation processes using different current densities. Figure 7 displays the correlation between the mean coating thickness and the current density. The cross-sectional morphology of the MAO coatings on both BM-MAO and WZ-MAO exhibits a similar structure, featuring a loose outer layer and a dense inner layer. The growth of the coating, both inward and outward, results in an uneven thickness distribution. Moreover, a metallurgical bond is formed between the dense layer and the substrate [37]. Figure 7 reveals that the thickness of the BM-MAO coating increases with current densities. Specifically, the average coating thickness increases from 7.7 to 12.7 μm as the current density rises from 10 A/dm^2 to 16 A/dm^2. A higher current density produces a more vigorous micro-arc oxidation reaction, thus fostering the generation of molten materials and thicker coatings.

Figure 8 shows that the thickness of the MAO coating in the WZ region first increases and then decreases, reaching its maximum at a current density of 12 A/dm^2. This is because the coarse metastable needle shaped α′ martensite formed in the WZ region (Figure 2) during the welding process has a relatively lower breakdown voltage compared to other regions. Under the same process, the micro arc oxidation time that occurs in the WZ region is longer and the energy density is higher compared to BM regions, resulting in the maximum coating thickness in the WZ region. However, as the current density further increases, the WZ region experiences continuous breakdown and detachment of the coating at high current densities, and the thickness of the coating begins to decrease. At the same time, the

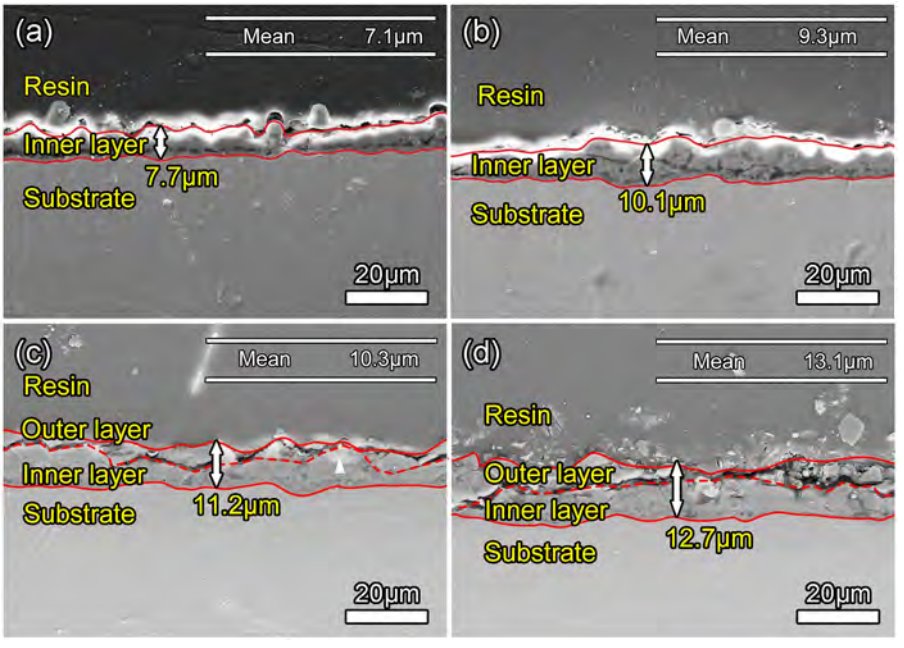

Figure 7. Cross-sectional morphology of BM-MAO coatings at different current densities: (a) 10 a/dm^2; (b) 12 a/dm^2; (c) 14 a/dm^2; (d) 16 a/dm^2.

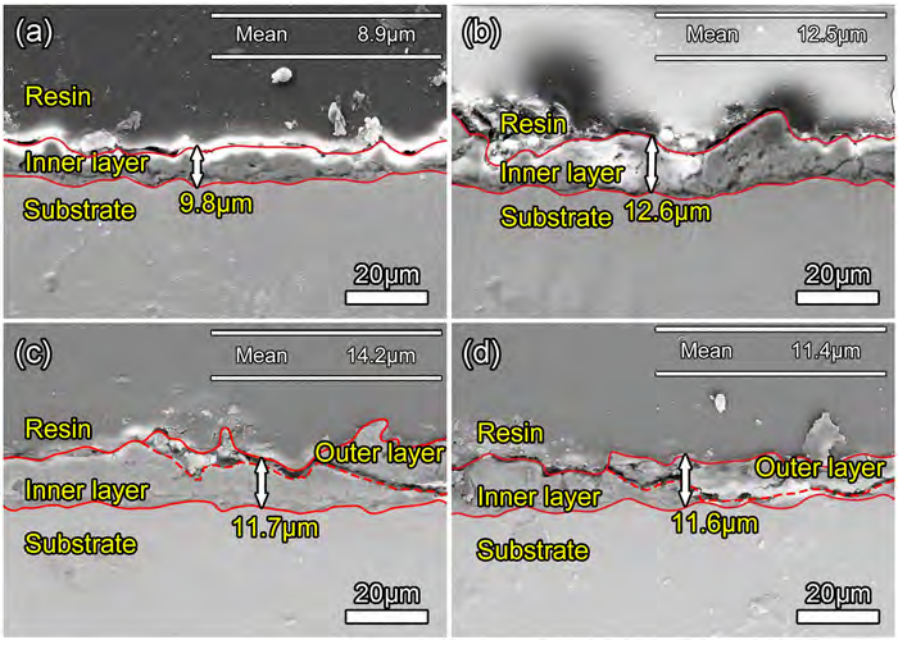

Figure 8. Cross-sectional morphology of WZ-MAO coating at different current densities: (a) 10 a/dm^2; (b) 12 a/dm^2; (c) 14 a/dm^2; (d) 16 a/dm^2.

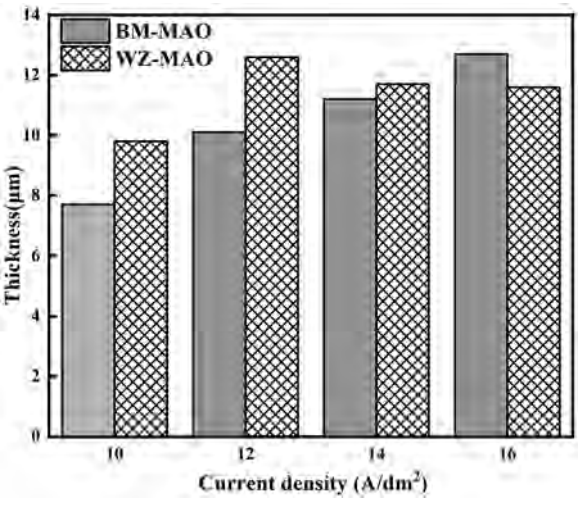

Figure 9. Variation of MAO coating thickness with current densities.

maximum thickness of the film layer begins to decrease at a current density of 12 A/dm^2, and the minimum thickness begins to decrease at a current density of 14 A/dm^2.

Furthermore, it can be observed that as the current density increases, the defects in the coating first increase and then decrease. Microcracks can be observed in the coating prepared at a current density of 12 A/dm^2. When the current density is greater than 12 A/dm^2, no defects such as pores are observed in the coating, indicating that at high current densities, the energy of micro arc oxidation is greater, resulting in an increase in the melting area of the coating and an increase in the pore size (Figure 5g). The occurrence of self-sealing pores in the coating increases, but it also indicates an increase in roughness. However, due to the significant thermal stress generated during the cooling process of the molten material, cracks appear on the surface of the coating, leading to the detachment of the coating, resulting in a continuous decrease in coating thickness.

Figure 9 shows the thickness variation trend of BM-MAO and WZ-MAO coatings. The increase in current density increases the intensity of MAO reaction, and the thickness of BM-MAO coating increases with the increase of current density, while the thickness of WZ-MAO coating first increases and then decreases. When the current density is 12 A/dm^2, the thickness of MAO coating is relatively large, and there are fewer cracks in the coating that bond well with the substrate. When the current density is greater than 12 A/dm^2, due to the relatively high energy density of micro arc oxidation, the melting area of the coating increases, and the occurrence of self-sealing pores increases. The coating continuously undergoes remelting and cooling, and the number of micro pores in the coating decreases. The pore size and surface roughness increase, and the defects in the inner layer are repaired. However, due to the cooling effect of the electrolyte on the molten material, a large thermal stress is generated, resulting in the breakdown and detachment of the coating, a decrease in thickness, obvious cracks in the cross section, and detachment of the film layer from the substrate. Due to the different microstructures of the BM

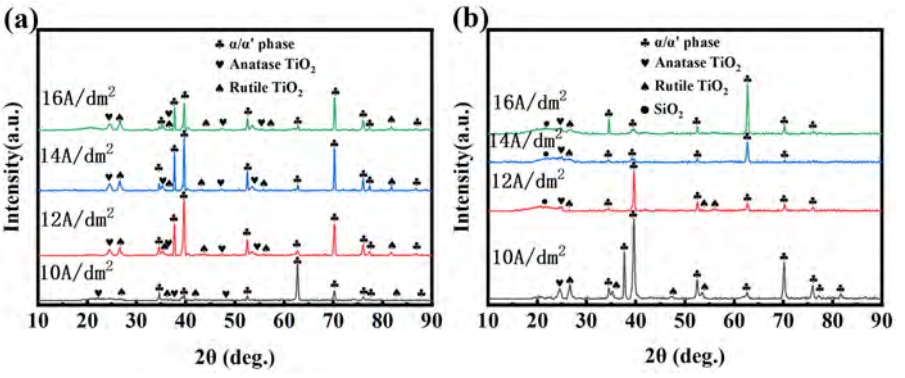

Figure 10. XRD spectra: (a) BM-MAO; (b) WZ-MAO at various current densities.

and the weld seam, the difficulty of micro arc oxidation varies. This results in different energy densities and coating thicknesses for the BM and weld seam under the same process. In order of difficulty, BM > WZ. This is because the closer to the center of the weld seam, the more needle shaped α′ martensite in the metastable state and the coarser the microstructure. Therefore, when the current density does not exceed 14 A/dm^2, the coating thickness and maximum coating thickness in each region show an upward trend, in the order of WZ > BM. When the current density is 16 A/dm^2, the larger energy density leads to the detachment of the WZ-MAO coating, resulting in a significant decrease in the thickness of the coating. The thickness of the BM-MAO coating shows an upward trend, with no inflection point displayed. This is mainly due to the relatively small degree of micro arc oxidation reaction occurring in this area, and the relatively small thermal stress generated during cooling. At this time, microcracks mainly occur (Figure 4g), and the breakdown and detachment phenomenon of the coating is not obvious.

3.4. Effects of current densities on the phase composition of MAO coatings

Figures 10 and 11 present the X-ray diffraction (XRD) spectra of the BM and WZ coatings at various current densities. The phase composition of the MAO coatings is consistent for different current densities in each respective region composed of both rutile and anatase forms of TiO_2. The α/α′ phase diffraction peak appears because the thin coating lets X-ray penetrate the MAO layer to reach the substrate. Figure 11a shows that the concentration of stable rutile TiO_2 in the BM region increases with current densities, although it increases slowly after 12 A/dm^2. Figure 11b shows that the maximum concentration of rutile TiO_2 in the WZ region occurs at 10 A/dm^2, with diffraction peaks of SiO_2 becoming noticeable at 12–16 A/dm^2. As the current density continues to rise, the rutile TiO_2 content decreases (Figure 11b), and SiO_2 diffraction peaks emerge at this juncture. The surge observed at 16 A/dm^2 corresponds to the most intense reaction phase and the thermal accumulation effect, facilitating the phase transformation of anatase TiO_2 to other phases. Compared to the BM-MAO coating, the concentration of stable rutile TiO_2 in WZ-MAO coating is smaller at current densities of 12 – 16 A/dm^2.

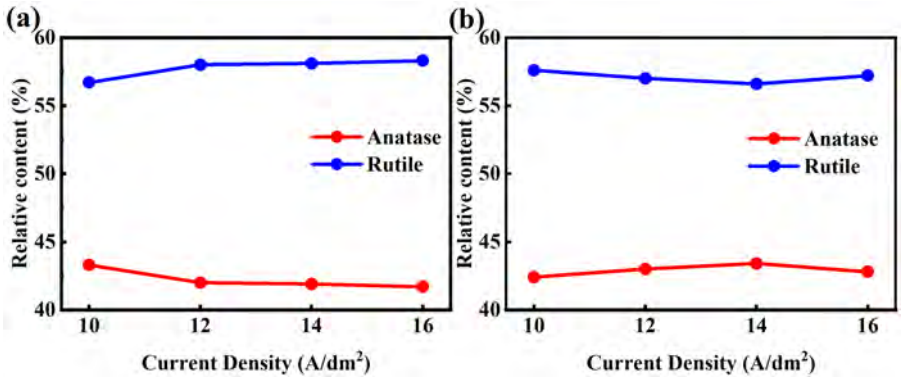

Figure 11. Relative content of rutile and anatase TiO_2: (a) BM-MAO and (b) WZ-MAO at different current densities.

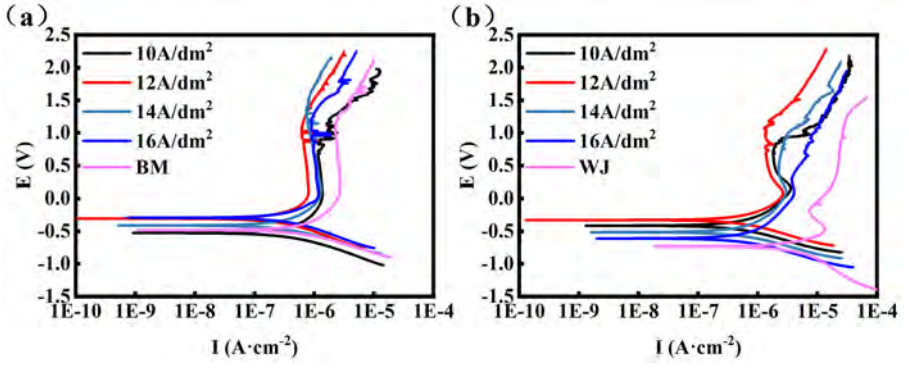

Figure 12. Kinetic potential polarization curves of BM and WJ in 3.5 wt.% NaCl solution before and after preparation of MAO coating: (a) BM; (b) WJ.

3.5. Effects of current densities on corrosion resistance

3.5.1. Dynamic potential polarization

Figure 12 shows the dynamic potential polarization curves of the BM and WJ without micro arc oxidation treatment, as well as the BM and WJ treated with micro arc oxidation at different current densities (10, 12, 14, 16 A/dm^2), with the corresponding fitted results shown in Table 3. Table 3 demonstrates a significant reduction in the self-corrosion current density in the BM region by an order of magnitude, whereas in the WJ region, the reduction is two orders of magnitude. There is a notable enhancement in the self-corrosion potential in both regions. This improvement in corrosion resistance due to the MAO coatings can be linked to their effectiveness in slowing erosion and mitigating galvanic coupling corrosion between the BM and WJ regions, thereby offering enhanced protection for the WJ region. Table 3 shows that there is not much difference in the corrosion resistance of the BM-MAO and WJ-MAO coatings under different current densities. Compared to the others, the corrosion resistance is a little better at current densities of 12 A/dm^2 and 14 A/dm^2.

Table 3. Fitted polarization results before and after MAO.

Sample	Ecorr/V	Icorr/A·cm^{-2}
BM	−0.482	1.08×10^{-6}
BM-MAO-10 A/dm^2	−0.525	5.563×10^{-7}
BM-MAO-12 A/dm^2	−0.307	6.169×10^{-7}
BM-MAO-14 A/dm^2	−0.411	4.434×10^{-7}
BM-MAO-16 A/dm^2	−0.294	8.031×10^{-7}
WJ	−0.733	1.14×10^{-5}
WJ-MAO-10 A/dm^2	−0.415	6.601×10^{-7}
WJ-MAO-12 A/dm^2	−0.388	6.838×10^{-7}
WJ-MAO-14 A/dm^2	−0.399	5.994×10^{-7}
WJ-MAO-16 A/dm^2	−0.434	6.761×10^{-7}

3.5.2 Electrochemical impedance spectroscopy (EIS)

Figure 13 displays the EIS curves for the BM and WJ without micro arc oxidation treatment, as well as the BM and WJ treated with micro arc oxidation at different current densities (10, 12, 14, 16 A/dm^2), with the corresponding fitted results shown in Table 4. The Nyquist plots of BM-MAO and WJ-MAO reveal two capacitive loops at current densities of 10 A/dm^2 and 12 A/dm^2, suggesting a bilayer coating. However, the MAO coatings fabricated at current densities of 14 A/dm^2 and 16 A/dm^2 exhibit only a single capacitive loop. The impedance |Z| at a frequency of 0.1 Hz of the BM-MAO coatings is similar. However, that of the WJ-MAO coatings follows the order: |Z| at 12 A/dm^2 > |Z| at 10 A/dm^2 > |Z| at 14 A/dm^2 > |Z| at 16 A/dm^2. This sequence signifies that the coatings produced at a current density of 12 A/dm^2 possess superior corrosion resistance. Moreover, the |Z| values of BM-MAO coatings are higher than those of WJ-MAO coatings, indicating better corrosion resistance. This enhanced performance is attributed to the more homogeneous nature of the coating in the BM region with less defects.

According to Table 4, the resistances R_1 and R_2 generally exhibit a trend of initial increase and then decrease with current densities. Notably, R_1 and R_2 of the MAO coating show a peak at a current density of 12 A/dm^2. The resistances R_1 and R_2 of BM-MAO coatings are bigger than those of WJ-MAO coatings, indicating better corrosion resistance. Moreover, R_1 of the WJ-MAO coatings at current densities of 14 and 16 A/dm^2 is very low because at high current densities, the coating is broken down and detached, and there is a very loose outer layer or almost no outer layer (e.g. Figures 7 and 8).

Table 4 also shows that the constant phase element (CPE_2-Q_2) of the BM-MAO coatings is lower than that of the WJ-MAO coatings and reaches its lowest value at a current density of 12 A/dm^2, whereas for the WJ-MAO coating, the minimum CPE_2-Q_2 is observed at a current density of 10 A/dm^2. This discrepancy arises from the more vigorous MAO process in the WZ region. Despite a decrease in porosity, there is a notable increase in the surface roughness and consequently, an expansion in the surface area for WJ-MAO coatings at different current densities. This leads to an enhanced surface capacitance which displays a consistent upward trend. Therefore, the absorbability of dielectric charges is higher to facilitate charge transfer and corrosive dissolution of metal ions. However, with regard to the BM-MAO coatings, the small pore size allows less corrosion solution to penetrate the pores. During electrochemical corrosion, the migration speed of ions is much slower than

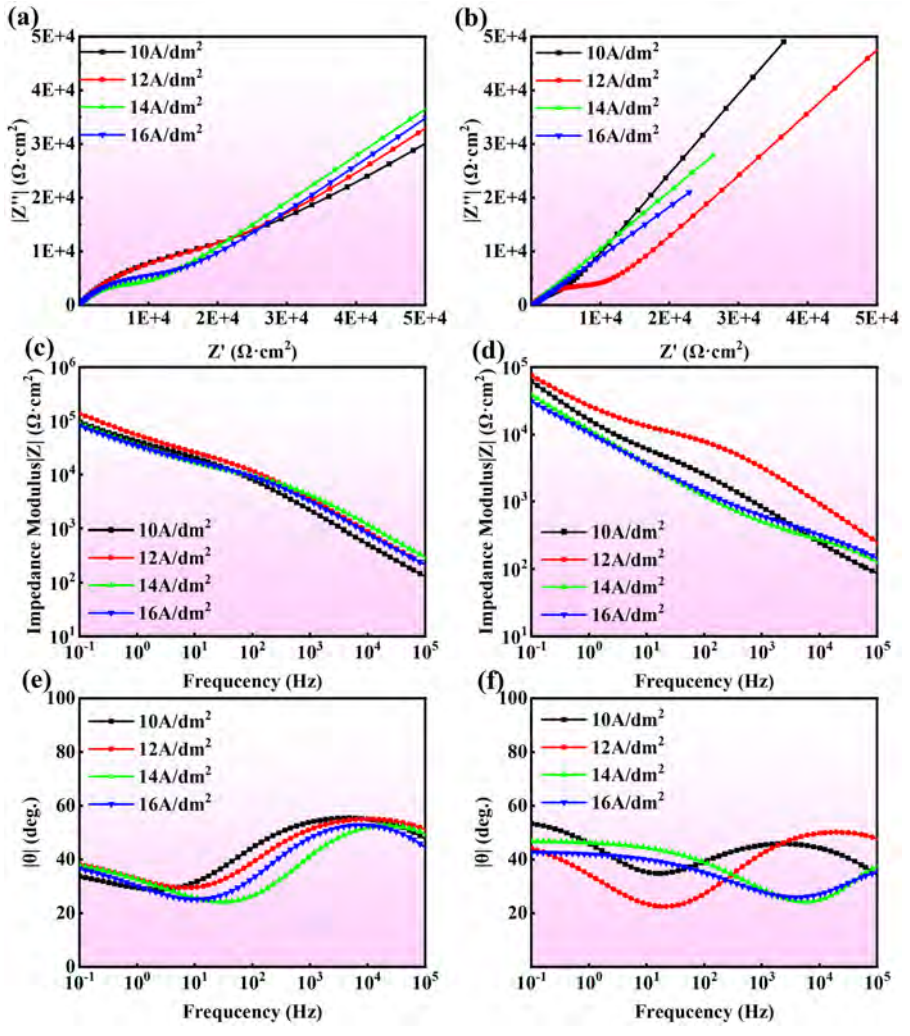

Figure 13. (a, c, e) Nyquist, impedance modulus and phase angle plots of BM-MAO; (b, d, f) Nyquist, impedance modulus and phase angle plots of WJ-MAO.

the movement speed of electrons, leading to the formation of a double dielectric layer structure at the pores. The presence of a large number of pores results in a double dielectric layer structure on the surface of the coating, where both dense and dispersed layers coexist. Due to the stability of the double dielectric layer structure, the coating with higher porosity and smaller average pore size has good corrosion resistance.

4. Discussion

This study explores the impact of the MAO current density on the microstructure of MAO coatings in the BM region and WZ of Ti6Al4V electron beam WJ as well as the corrosion resistance of the BM coating and WJ-coating. The porosity of

Table 4. Fitted EIS results of BM-MAO and WJ-MAO coatings for different current densities.

	Parameters						
		CPE_1			CPE_2		
Samples	R_S ($\Omega \cdot cm^2$)	Q_1	N_1	R_1 ($k\Omega \cdot cm^2$)	Q_2	N_2	R_2 ($M\Omega \cdot cm^2$)
BM-MAO-10 A/dm^2	29.02	1.45×10^{-6}	0.65	22.76	1.47×10^{-5}	0.43	2.285×10^{7}
BM-MAO-12 A/dm^2	30.21	8.1×10^{-7}	0.65	27.35	9.41×10^{-6}	0.44	2.875×10^{7}
BM-MAO-14 A/dm^2	33.03	6.9×10^{-7}	0.64	10.81	1.51×10^{-5}	0.46	1.885×10^{7}
BM-MAO-16 A/dm^2	61.11	9.1×10^{-7}	0.65	14.17	1.67×10^{-5}	0.46	1.575×10^{7}
WJ-MAO-10 A/dm^2	31.81	8.18×10^{-6}	0.56	8.47	1.48×10^{-5}	0.65	2.085×10^{7}
WJ-MAO-12 A/dm^2	34.56	1.22×10^{-6}	0.61	11.44	1.77×10^{-5}	0.44	2.795×10^{7}
WJ-MAO-14 A/dm^2	30.12	2.91×10^{-6}	0.64	0.24	3.31×10^{-5}	0.52	2.715×10^{7}
WJ-MAO-16 A/dm^2	30.23	1.08×10^{-6}	0.65	0.34	3.95×10^{-5}	0.47	1.065×10^{7}

BM-MAO and WZ-MAO coatings decreases with increasing current densities. However, the porosity of BM-MAO coatings is higher than that of WZ-MAO coatings at different current densities. The average thickness of the BM-MAO coating progressively ascends from 7.7 to 12.7 μm with current densities. In comparison, the thickness of the WZ-MAO coating increases first and then decreases, showing a maximal thickness of 12.6 μm at a current density of 12 A/dm^2. This is due to the uneven microstructure of the welded joint, with more needle shaped α′ martensite in the WZ region at high energy than in the BM region. The BM-MAO coatings and WZ-MAO coatings are mainly composed of rutile TiO_2 and anatase TiO_2. The rutile TiO_2 in BM-MAO coating grows with current densities. In comparison, the content of rutile TiO_2 in WZ-MAO coating decreases first and then increases. For anatase TiO_2, they are reversed. The BM-MAO coatings and WJ-MAO coatings show much better corrosion resistance than BM and WJ without MAO, achieving optimal corrosion resistance at 12 A/dm^2. According to the analysis of the equivalent resistance and dielectric behavior, the corrosion resistance of the BM-MAO coatings is better than that of WJ-MAO coatings at different current densities.

Disclosure statement

No potential conflict of interest was reported by the author(s).

Funding

The paper was funded by the National Natural Science Foundation of China (No. 52375391), the City University of Hong Kong Donation Research Grants (DON-RMG 9229021 and 9220061).

References

[1] Chen GQ, Zhang G, Yin QX, et al. Microstructure evolution of electron beam welded joints of Ti-43Al-9V-0.3Y and Ti-6Al-4V alloys. Mater Lett. 2018;233:336–339. doi: 10.1016/j.matlet.2018.09.042.

[2] Zhao XL, Lu XH, Wang K, et al. Microstructure and mechanical properties of electron beam welded TC4 titanium alloy structure with backing plate. Mater Today Commun. 2023;35:106160. doi: 10.1016/j.mtcomm.2023.106160.

[3] Su ML, Li JN, Liu KG, et al. Mechanical property and characterization of TA1 titanium alloy sheets welded by vacuum electron beam welding. Vacuum. 2019;159:315–318. doi: 10.1016/j.vacuum.2018.10.027.
[4] Han X, Ma JX, Tian AX, et al. Surface modification techniques of titanium and titanium alloys for biomedical orthopaedics applications: a review. Colloids Surf B Biointerfaces. 2023;227:113339. doi: 10.1016/j.colsurfb.2023.113339.
[5] Zhu QQ, Yang XD, Lan HF, et al. Effect of solution treatments on microstructure and mechanical properties of Ti–6Al–4V alloy hot rolled sheet. J Mater Res Technol. 2023;23:5760–5771. doi: 10.1016/j.jmrt.2023.02.192.
[6] K VK, C GK, Rehman AU, et al. Effect of welding speed and post-weld heat treatment on microstructural and mechanical properties of alpha + beta titanium alloy EB welds. Fusion Sci Technol. 2024;80(2):166–177. doi: 10.1080/15361055.2023.2211723.
[7] Sandhya V, Sastry MNP, Reddy KHC. Influence of welding speed, voltage, and beam current on the microstructure and mechanical properties of electron beam-welded titanium radial joints. Mater Today: Proc. 2022;64:442–447.
[8] Gao FG, Sun ZJ, Yang SL, et al. Stress corrosion characteristics of electron beam welded titanium alloys joints in NaCl solution. Mater Charact. 2022;192:112126. doi: 10.1016/j.matchar.2022.112126.
[9] Zhang WY, Fan JK, Huang H, et al. Creep anisotropy characteristics and microstructural crystallography of marine engineering titanium alloy Ti6321 plate at room temperature. Mater Sci Eng A. 2022;854:143728. doi: 10.1016/j.msea.2022.143728.
[10] Yang X, Wang WL, Ma WJ, et al. Corrosion and wear properties of micro-arc oxidation treated Ti6Al4V alloy prepared by selective electron beam melting. Trans Nonferrous Met Soc China. 2020;30(8):2132–2142. doi: 10.1016/S1003-6326(20)65366-3.
[11] Fazel M, Shamanian M, Salimijazi HR. Enhanced corrosion and tribocorrosion behavior of Ti6Al4V alloy by auto–sealed micro-arc oxidation layers. Biotribology. 2020;23:100131. doi: 10.1016/j.biotri.2020.100131.
[12] Wang Y, Yu HJ, Chen CZ, et al. Review of the biocompatibility of micro-arc oxidation coated titanium alloys. Mater Des. 2015;85:640–652. doi: 10.1016/j.matdes.2015.07.086.
[13] Bai HQ, Zhong LS, Kang L, et al. A review on wear-resistant coating with high hardness and high toughness on the surface of titanium alloy. J Alloys Compd. 2021;882:160645. doi: 10.1016/j.jallcom.2021.160645.
[14] Wei P, Chen L, Li X, et al. Development of self-healing functional micro-arc oxidation coating on magnesium alloys: a review. J Adhes Sci Technol. 2024;38(7):991–1013. doi: 10.1080/01694243.2023.2251759.
[15] Sukuroglu EE, Farzi H, Sukuroglu S, et al. The effect of plasma electrolytic oxidation process parameters on the tribocorrosion properties of TiO_2 coatings. J Adhes Sci Technol. 2017;31(12):1361–1373. doi: 10.1080/01694243.2016.1256635.
[16] Shokouhfar M, Allahkaram SR. Effect of incorporation of nanoparticles with different composition on wear and corrosion behavior of ceramic coatings developed on pure titanium by micro arc oxidation. Surf Coat Technol. 2017;309:767–778. doi: 10.1016/j.surfcoat.2016.10.089.
[17] Sobolev A, Kossenko A, Borodianskiy K. Study of the effect of current pulse frequency on Ti-6Al-4V alloy coating formation by micro arc oxidation. Materials. 2019;12(23):3983. doi: 10.3390/ma12233983.
[18] Li G, Ma F, Liu P, et al. Review of micro-arc oxidation of titanium alloys: mechanism, properties and applications. J Alloys Compd. 2023;948:169773. doi: 10.1016/j.jallcom.2023.169773.
[19] Lan N, Yang W, Gao W, et al. Characterization of ta-C film on micro arc oxidation coated titanium alloy in simulated seawater. Diamond Relat Mater. 2021;117(1):108483. doi: 10.1016/j.diamond.2021.108483.
[20] Kaplan E, Sukuroglu EE, Cuvalci O. Investigation of characterization and tribological behavior of composite oxide coatings doped with h-BN and graphite particles on ZA-27 alloy by micro-arc oxidation. J Adhes Sci Technol. 2021;35(12):1305–1319. doi: 10.1080/01694243.2020.1843315.

[21] Yang Z, Yu M, Han C, et al. Evolution and corrosion resistance of passive film with polarization potential on Ti-5Al-5Mo-5V-1Fe-1Cr alloy in simulated marine environment. Corros Sci. 2023;221:111334. doi: 10.1016/j.corsci.2023.111334.
[22] Ma YH, Wu P, Mei JH, et al. Effects of Micro-Arc Oxidation Surface Treatment on the Corrosion Resistance of Ti-6Al-4V Electron-Beam-Welded Joints. Metals. 2023;13(7):1161. doi: 10.3390/met13071161.
[23] Matin R, Totik Y, Sukuroglu EE, et al. Effects of voltage on the components of surface integrity of Al2O3 ceramic coatings on AA2024 by plasma electrolytic oxidation. J Adhes Sci Technol. 2020;34(18):1971–1981. doi: 10.1080/01694243.2020.1742970.
[24] Chen L, Zhao R, Qi H, et al. Influence of voltage modes on microstructure and corrosion resistance of micro-arc oxidation coating on magnesium alloy. J Adhes Sci Technol. 2023;37(15):2232–2246. doi: 10.1080/01694243.2022.2122294.
[25] Wang P, Wei WX, Pu J, et al. Effect of current density on characteristics of 2024 aluminum alloy microarc oxidation coatings with titanium dioxide particles. Int J Electrochem Sci. 2019;14(5):4338–4349. doi: 10.20964/2019.05.30.
[26] Tang WX, Yan JK, Yang G, et al. Effect of electrolytic solution concentrations on surface hydrophilicity of micro-arc oxidation ceramic film based on Ti6Al4V titanium alloy. Rare Metal Mater Eng. 2014;43:2883–2888.
[27] Chong Y, Bhattacharjee Y, Tian YZ, et al. Deformation mechanism of bimodal microstructure in Ti-6Al-4V alloy: the effects of intercritical annealing temperature and constituent hardness. J Mater Sci Technol. 2021;71:138–151. doi: 10.1016/j.jmst.2020.08.057.
[28] Gong YB, Wang SL, Li J. Microstructure evolution of thick TC4 titanium alloy vacuum electron beam welded joint. Trans China Weld Inst. 2017;38(09):91–96. +133.
[29] Sun W, Wang S, Wu M, et al. Revealing tensile behaviors and fracture mechanism of Ti–6Al–4V titanium alloy electron-beam-welded joints using microstructure evolution and in situ tension observation. Mater Sci Eng A. 2021;824:141811. doi: 10.1016/j.msea.2021.141811.
[30] Yang Y, Wu H. Effects of current density on microstructure of titania coatings by micro-arc oxidation. J Mater Sci Technol. 2012;28(4):321–324. doi: 10.1016/S1005-0302(12)60062-0.
[31] Cui XJ, Yang RS, Liu CH, et al. Structure and corrosion resistance of modified micro-arc oxidation coating on AZ31B magnesium alloy. Trans Nonferrous Met Soc China. 2016;26(3):814–821. doi: 10.1016/S1003-6326(16)64172-9.
[32] Fernández-López P, Alves SA, Azpitarte I, et al. Corrosion and tribocorrosion protection of novel PEO coatings on a secondary cast Al-Si alloy: influence of polishing and sol-gel sealing. Corros Sci. 2022;207:110548. doi: 10.1016/j.corsci.2022.110548.
[33] Duarte LT, Bolfarini C, Biaggio SR, et al. Growth of aluminum-free porous oxide layers on titanium and its alloys Ti-6Al-4V and Ti-6Al-7Nb by micro-arc oxidation. Mater Sci Eng C Mater Biol Appl. 2014;41:343–348. doi: 10.1016/j.msec.2014.04.068.
[34] Jayaraj RK, Malarvizhi S, Balasubramanian V. Optimizing the micro-arc oxidation (MAO) parameters to attain coatings with minimum porosity and maximum hardness on the friction stir welded AA6061 aluminium alloy welds. Defence Technol. 2017;13(2):111–117. doi: 10.1016/j.dt.2017.03.003.
[35] Cheng YL, Wu XQ, Xue ZG, et al. Microstructure, corrosion and wear performance of plasma electrolytic oxidation coatings formed on Ti–6Al–4V alloy in silicate-hexametaphosphate electrolyte. Surf Coat Technol. 2013;217:129–139. doi: 10.1016/j.surfcoat.2012.12.003.
[36] Wu B, Li JW, Tang ZY. Study on the electron beam welding process of ZTC4 titanium alloy. Rare Metal Materials and Engineering. 2014;43(4):786–790. doi: 10.1016/S1875-5372(14)60084-9.
[37] Li JN, Li JS, Qi WJ, et al. Characterization and mechanical properties of thick TC4 titanium alloy sheets welded joint by vacuum EBW. Vacuum. 2019;168:108812. doi: 10.1016/j.vacuum.2019.108812.